The Eurasia Proceedings of Science, Technology, Engineering & Mathematics (EPSTEM)
ISSN: 2602-3199

The Eurasia Proceedings of Science, Technology, Engineering and Mathematics (EPSTEM), 2025

Volume 37, Pages 444-456

ICEAT 2025: International Conference on Engineering and Advanced Technology

Band Pass Filter Utilizing a Stepped Impedance Resonator for Modern Wireless Communication System

Enas S. Mohammed
University of Technology - Iraq

Mohammed F. Hasan
University of Technology - Iraq

Jabber K. Mohammed
University of Technology - Iraq

Abstract: This study presents the design and evaluation of a second-order dual-band bandpass filter (DBPF) for modern wireless communication systems. The proposed filter employs meandered-shaped stepped impedance resonators (MSIRs) to achieve compact size and enhanced performance. The first band operates at 2.6 GHz with a fractional bandwidth (FBW) of 18%, while the second band is centered at 4.37 GHz with an FBW of 11%. Three transmission zeros (TZs) are strategically positioned to improve the filter's selectivity. The filter is implemented on Rogers RO 4350C substrate with $\varepsilon_r = 3.66$, $\tan \delta = 0.001$, and thickness $h = 0.762$ mm, resulting in an overall filter area of 49×30 mm² ($0.7\lambda g \times 0.47\lambda g$ at 2.6 GHz). CST Studio Suite 2019 was utilized for electromagnetic analysis. Simulation results demonstrate low insertion loss (IL) and high return loss (RL) at both operating bands, achieving IL of 0.2 dB and RL of 16.7 dB for the first band, and IL of 0.6 dB and RL of 11.3 dB for the second band. The transmission zeros are located at 1.93, 3.71, and 4.83 GHz, respectively. The proposed filter operates with quasi-independent dual-band functionality, which can be controlled by adjusting the section lengths of the SIR.

Keywords: Dual-band pass filter (DBPF), Stepped ımpedance resonator (SIR), Meandered shaped stepped impedance resonators (MSIRs)

Introduction

Modern wireless communication systems require efficient filtering components that can operate across multiple frequency bands while maintaining compact form factors (Basheer et al., 2022; Khani et al., 2022). The increasing demand for multi-band operation in contemporary RF and microwave applications has driven the development of dual-band bandpass filters (DB-BPFs) as essential components in wireless infrastructure, including WiFi networks, radar systems, and communication transceivers. Traditional single-frequency filtering approaches are inadequate for current multi-band wireless architectures. Conventional bandpass filtering structures typically employ parallel-coupled transmission lines, resulting in substantial physical footprints that limit their applicability in compact systems. Size reduction represents a critical design challenge, as filtering elements must provide excellent performance while occupying minimal space (Radhi & Fadhil, 2023). Numerous filter designs have been proposed to meet the growing demands of RF and microwave systems. These include bandstop filters (Li et al., 2020), tunable filters (Gao et al., 2019), reconfigurable filters (Bandyopadhyay et al., 2021), low-pass filters with strong out-of-band suppression (Alizadeh Pahlavani et al., 2020), and various bandpass filters (Hu et al., 2020). Dual-band bandpass filters (DB-BPFs) have attracted attention due to their suitability for multi-band RF transceivers. For instance, a dual-wideband BPF based on cross-shaped resonators Bi et al. (2020) and another

using hexagonal SRR structures (Troudi et al., 2020) have been developed. A major design challenge is size reduction, especially as traditional parallel-coupled line filters (Tsai & Lee, 2007; Marin et al., 2017) occupy large areas. Hairpin and meandered resonators (Sanchez-Renedo et al., 2013; Ma et al., 2007; Marzah & Aziz, 2018) have offered more compact alternatives, though some suffer from high insertion loss or complex fabrication. Substrate Integrated Waveguide (SIW) technology has shown significant potential for miniaturization (Pu et al., 2019; Riaz et al., 2016), with designs like lateral stub-loaded SIW cavities achieving compact structures. Stepped Impedance Resonators (SIR), introduced by Makimoto et al. (1980), have also gained popularity for their reduced size and improved spurious response control. For example, the design in (Orellana et al., 2017) uses slow-wave techniques to shrink dimensions but comes at higher manufacturing cost. This study aims to develop a compact, cost-effective filtering structure with enhanced selectivity and simplified fabrication requirements.

The research objective of this investigation focuses on developing a filtering architecture that fulfills specified performance parameters through economical manufacturing processes, simplified topological configurations, superior frequency discrimination characteristics, and dimensional optimization. The development of space-efficient of DB-BPFs exhibiting exceptional selectivity performance and minimal signal attenuation continues to present significant engineering challenges. Traditional implementation approaches frequently result in oversized configurations or intricate design complexities, while numerous established size reduction methodologies necessitate compromises between operational performance, fabrication costs, or production feasibility.

The simultaneous realization of both narrow-band and broad-band transmission characteristics with robust spurious signal rejection within streamlined, miniaturized architectures remains an unresolved challenge in contemporary filtering system design. The architectural configuration presented in this investigation derives from second-order hairpin resonator topologies, wherein stepped-impedance resonator elements are arranged in hairpin geometrical formations. For design verification purposes, the developed filtering structure achieves fractional bandwidth characteristics of 18.1% and 11.8% through SIR-based implementation. The filtering circuit has been realized on Rogers RO4003C substrate material featuring 0.762mm thickness, characterized by 3.66 with a relative permittivity and 0.0037with loss tangent. The substrate configuration has been computationally modeled and analyzed through electromagnetic simulation software.

Filter Design Methodology

Design Specifications

This article is aimed at providing high selectivity, and low insertion and quasi- band constructed on the challenges placed by many the requirements. The futures of BPF construction are mentioned in Table 1.

Table 1. Specifications for proposed filter.

F_o (GHz)	BW	RL (aB)	IL(dB)	Order (N)	Application
2.7	18 %	16.7	0.2	2	4G & 5G mobile broad-band services Wireless Netwrok with businesses and organizations
4.37	11%	11.3	0.6	2	

Stepped Impedance Resonator Theory

Stepped-impedance resonating structures encompass three fundamental categories: quarter-wavelength resonant elements, half-wavelength resonant configurations, and full-wavelength resonant topologies. The geometric arrangement of a half-wavelength symmetrical (SIR.). architecture illustrated in Figure1 (SIR) configuration comprises dual transmission line segments exhibiting distinct characteristic impedance values Z1 and Z2, corresponding electrical phase lengths θ1 and θ2, and respective admittance parameters Y1 and Y2. The transmission matrix representation for this non-uniform structural configuration can be derived as:

$$\begin{bmatrix} A & B \\ C & D \end{bmatrix} = \begin{bmatrix} \cos\theta_2 & j\mathrm{Z}_1 \sin\theta_2 \\ j\frac{\sin\theta_2}{\mathbb{Z}_2} & \cos\theta_2 \end{bmatrix} \begin{bmatrix} \cos 2\theta_1 & j\mathbb{Z}_2 \sin 2\theta_1 \\ j\frac{\sin 2\theta_1}{\mathrm{Z}_1} & \cos 2\theta_1 \end{bmatrix} \begin{bmatrix} \cos\theta_2 & j\mathrm{Z}_1 \sin\theta_2 \\ j\frac{\sin\theta_2}{\mathbb{Z}_2} & \cos\theta_2 \end{bmatrix} \quad (1)$$

Input Admittance Y_{in} of the Asymmetrica SIR show as :

$$Yin = jY2\ \frac{2(\mathrm{K}\tan\theta_1+\tan\theta_1)(\mathrm{K}-\tan\theta_1.\tan\theta_2)}{\mathrm{K}(1-\tan\theta_1{}^2)(1-\tan\theta_2{}^2)-2(1+\mathrm{K}^2).\tan\theta_1\ \tan\theta_2} \quad (2)$$

Since .K means the characteristic. impedance ratio. (Z2/Z1), the resonance state can be gained when Yin is being zero.

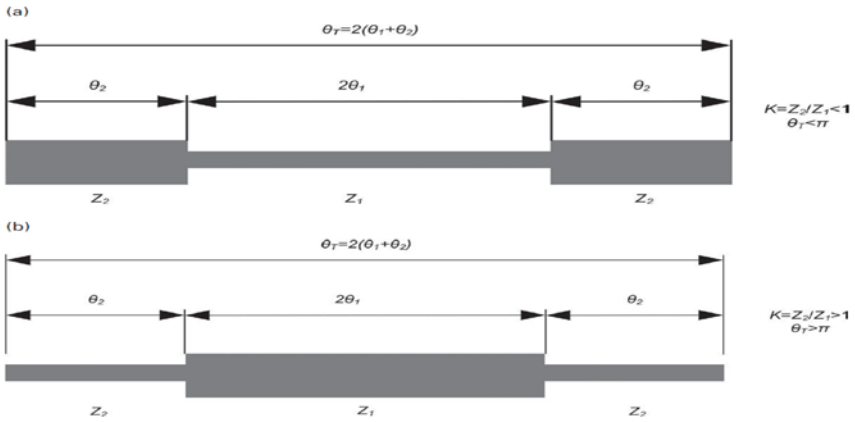

Figure 1. Premier structure of the half-wave length SIR.

Figure 2 demonstrates several dual-mode resonators that are utilized in multiband filter design. (CrnojevićBengin, 2015) provides resonant. state for λ/4-SIR (Figure2a).

$$K = \tan\theta_1 \tan\theta_2 \quad (3)$$

Since, K = Y1/Y2, Y1 and Y2 are characteristic admittance. $\theta 1$ and $\theta 2$ mean the lengths Electrically .
Owing to symmetry in SLR, Resonator can be analyzed by (even /odd) modes (Crnojević-Bengin, 2015). Even mode and Odd mode of the input admittances Y_{ine} & Y_{ino} for open stub SLR intended as (Bi et al., 2022)

$$Yine = jY1\ \frac{2y1\tan\theta_1+y2\tan\theta_2}{2y1+y2\tan\theta_1\ \tan\theta_2} \quad (4)$$

$$Yino = jY1\frac{1}{\tan_{\theta 1}} \quad (5)$$

In this context, Y with θ denotes typical admittance and electrical length. Resonance occurs when Im (Y_{in}) equals zero . The prototype exhibited two resonances Frequencies (f_e , f_o,) which could be designed as follows:

$$\tan\theta_1 = \infty \Rightarrow \theta_1 = \frac{\pi}{2} + n\pi \quad (6)$$

One definition of the transmission line's electrical length is

$$\theta_i = \beta L_i = \frac{2\pi f\sqrt{\varepsilon eff}}{c} L_i \quad (7)$$

Since L_i refer to physical length with TZ i, and f is means resonant frequency, εeff means effective relative permittivity, while C means light velocity in the vacuum. Replacing (6) in (7) confer the odd-mode resonant frequency As :

$$fo = \frac{(2n+1)\,c}{4L1\sqrt{\varepsilon eff}} \quad (8)$$

For Yin,e = 0

$$\cot(\theta 1)\tan(\theta 2) = -\frac{2y1}{y2} \quad (9)$$

If we let Y2 = 2Y1, The resonant state can be deduced as follows

$$\tan(\theta 2) = -\tan(\theta 1)$$
$$\Rightarrow \theta 2 = n\pi - \tan{-1}\,[\tan(\theta 1)] \quad (10)$$
$$\Rightarrow \theta 2 + \theta 1 = n\pi$$

This interduce the even-mode resonant frequency:

$$fe = \frac{nc}{2\,(L1 + L2)\sqrt{\epsilon eff}} \tag{11}$$

Likewise, we can figure out a short stub's even mode or odd mode resonant frequency SLR. The input admittances Yin,e and Yino considered as (Bi et al., 2022)

$$Yine = jY1\ \frac{2y1\tan\theta_1\tan\theta_2+y2}{2y1\tan\theta_2+y2\tan\theta_1} \tag{12}$$

$$Yino = jY1\frac{1}{tan_{\theta 1}} \tag{13}$$

Similar to open-stub SLR, the odd Mode resonant frequency is computed (Equation. 8). We have for even-mode resonance

$$Yin,e = 0 \Rightarrow \tan(\theta 1)\tan(\theta 2) = \frac{2y2}{y1} \tag{14}$$

If we let Y2 = 2Y1, the resonance situation can be inferred as

$$\tan(\theta 1)\tan(\theta 2) = 1$$
$$\Rightarrow\ \theta_1 + \theta_2 = \frac{\pi}{2} + n\pi \tag{15}$$

This primes to even mode of resonant frequency:

$$Fe = \frac{(2n + 1)\,c}{4(L1+1)\sqrt{\varepsilon eff}} \tag{16}$$

Something mentionable, f_{sn}(n = 1, 2, 3...) is the specious resonance frequency, and the first specious resonance happens at :

$$\tan\theta s1 = \infty \tag{17}$$

the initial spurious frequency with The electrical length at fs1 is denoted by θs1. Equations (3) and (4) give us:

$$\frac{f_{s1}}{f_o} = \frac{\theta_{s1}}{\theta_o} = \frac{\pi}{2tan^{-1}\sqrt{K}} \tag{18}$$

Equation (5) makes it evident that the impedance ratio K can regulate the false response.
It is possible to compute even Mode and odd mode input admittances (refer to Figures. 3(a , b)) as

$$Yin,\ 1 = jY1(2Y1\tan\theta1\tan\theta3\ -\ Y3)/(2Y1\tan\theta3\ +\ Y3\tan\theta1) \tag{19}$$

$$Yin,e = jY2(Yin,1\ +\ jY2\tan\theta2)/(Y2\ +\ jYin,1\tan\theta2) \tag{20}$$
$$Yin,o = -jY2\ \ k - tan\emptyset2tan\emptyset1`/\ tan\emptyset1` + ktan\theta2` \tag{21}$$

where $K = \frac{y2}{y1} = \frac{z2}{z1}$ $\quad \theta'1 = \beta$ (L1/2) , $\theta2 = \beta$L2 , $\theta3 = \beta$L3.

Equation (17) regulates 1st resonant frequency (f_1) which could be gotten with resonance state presented in Equation (12). So f1 is associated factors K, θ' 1 (L1), $\theta2$ (L2). Equation (20) presents two other frequencies and f2 and f3 beneath condition Yin,e = 0.

$$\tan\theta3 = \frac{y1y3-y2y3tan\emptyset1`\,tan\emptyset2}{2y1^2\,tan\emptyset1+2y1y2tan\emptyset2} = \frac{kk1-k1tan\emptyset1tan\emptyset2}{2ktan\emptyset1`+2tan\emptyset2}, \text{ where } k = \frac{y3}{y1}$$

The primary benefit of implementing SIR configurations in this architectural approach lies in achieving multiple resonant frequency responses within miniaturized structural dimensions. The cyclical characteristics of the tangent function (tan θ) generate unwanted harmonic frequency components (Khani et al., 2020). Figure 4 demonstrates three normalized parasitic resonant frequency values (fsp) corresponding to the λ/2-SIR topology, revealing that

spurious resonance spacing expands as the K parameter value diminishes and contracts with elevated K parameter values (Khani et al., 2020; Riaz et al., 2016).

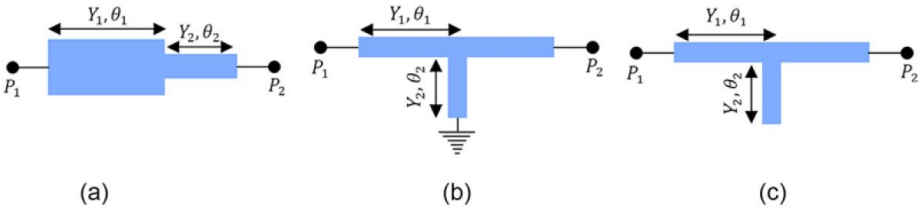

Figure 2. (a) λ/4-SIR, (b) short end.SLR (c) open end.SLR.

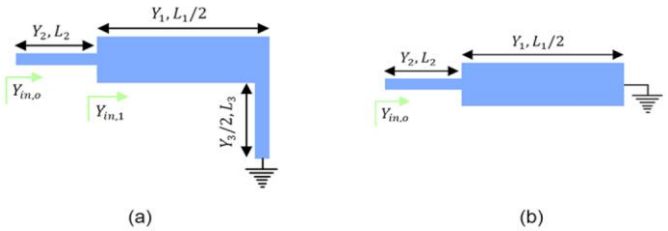

Figure 3. Identical circuit for the suggested SI-SLR structure. Even-mode (a) and odd .mode (b)

Results and Discussion

CST porgram used to compute the results for filter simulation, resulting in the design that incorporates two symmetric E-shaped stepped impedance resonators (SIR). The bandpass filter specifications are a center frequency of f_0 =(5.5 , 7.7) GHz, with FBW = (20% , 15%,) and a passband ripple of LAr = 0.2 dB . The filter order determined as second band, and. the configuration typical filter is shown on Figure. 5.a. A filter may be change position band to (SIR) on excuse of the distinct length coupling scheme.

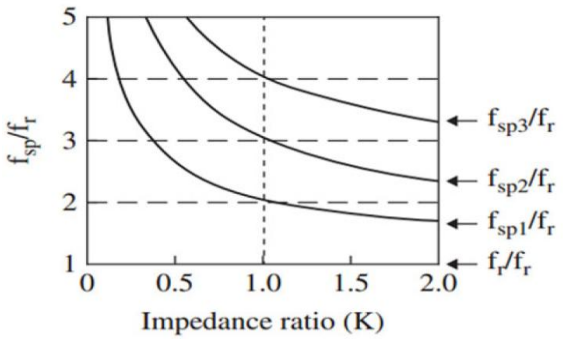

Figure 4. Specious resonance is shown. wavelength of λ/2-SIR (Seddiki et al., 2023).

among Z1 and Z2 units. The geometries of stepped impedance resonator is shown in Figure 5. The size of the structure is w1=2.5 , w2=1.4, L1 =18, L2=2, L3=2, L4=10, and gap between SIR G=0.1 (where all dimensions in mm) in the central frequency with the first passband (5.5 GHz) , second passband (7.5 GHz), third passband, the λg which means guided wavelength of the 50-. Ω microstrip line over the substrate referred to Alizadeh Pahlavani et al. (2020):

$$\lambda_g = \frac{\lambda_o}{\sqrt{\epsilon_{reff}}} \tag{6}$$

At Figure 5.b displays the frequency responses that correspond to S11 and S21.The findings depicted in Figure 5 indicate that the bandpass filters derived from the initial meander -shape geometry iterations exhibit second-band characteristics, with transmission zeros situated at the first two bands, specifically at 5.5 GHz and 7.5 GHz, respectively. Simultaneously, there exists effective isolation among the two passbands. The filter was designed using the CST Roggerv43035c substrate, which has ϵr of 3.66 , h =.762 mm, and tans = 0.0037. Figure 5 illustrates the simulation of the frequency response generated by the filter. The simulated 3-dB FBW for the passband, focusing at 5.5 GHz, is 20% dB/GHz, while at 7.7 GHz, it is 15%. The IL is 0.4 dB at 5.5 GHz and 0.6 dB at 7.5 GHz, while the RL exceeds 27 dB at 5.5 GHz and surpasses 12.3 dB at 7.7 GHz. We note from the

results high selectivity over all , in band second , match , return loss , insertion loss is weak , We can improve results in next section.

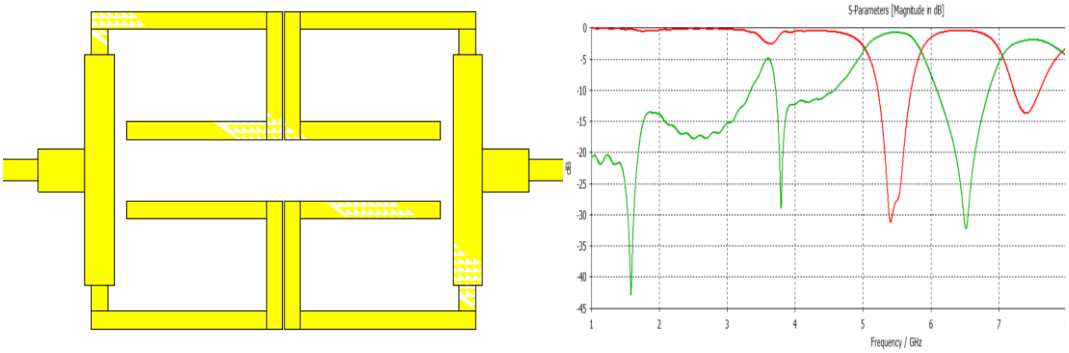

Figure 5. Right) Layout of second-order BPF, Left) Simulated S-parameters of BPF.

For enhanced understanding of the filtering performance characteristics, surface current density analysis serves as an effective evaluation methodology. Figure (7) illustrates the current density distribution patterns across the filter surface at frequencies within and beyond the transmission band. The initial out-of-band current density evaluation was conducted at 1.5GHz, as depicted in Figure (7-a). Current discontinuity phenomena are distinctly observable. At the secondary feeding port, current density approaches zero. The in-band frequency analysis at 2.6GHz presented in Figure (4.7-b) exhibits uniform current density distribution throughout the filtering structure with substantially elevated current magnitude values. The current density characteristics at the final out-of-band frequency shown in Figure (4.7-c), corresponding to 3GHz, demonstrate significantly reduced current values across the entire structural configuration. Complete current extinction occurs at the secondary feeding element. These analytical findings validate the overall frequency response characteristics of the developed filtering structure presented in Figure (6). Figure 7 depict the surface current distributions, with the red spots representing for highest level of coupling impact and blue spots representing the lowest level.

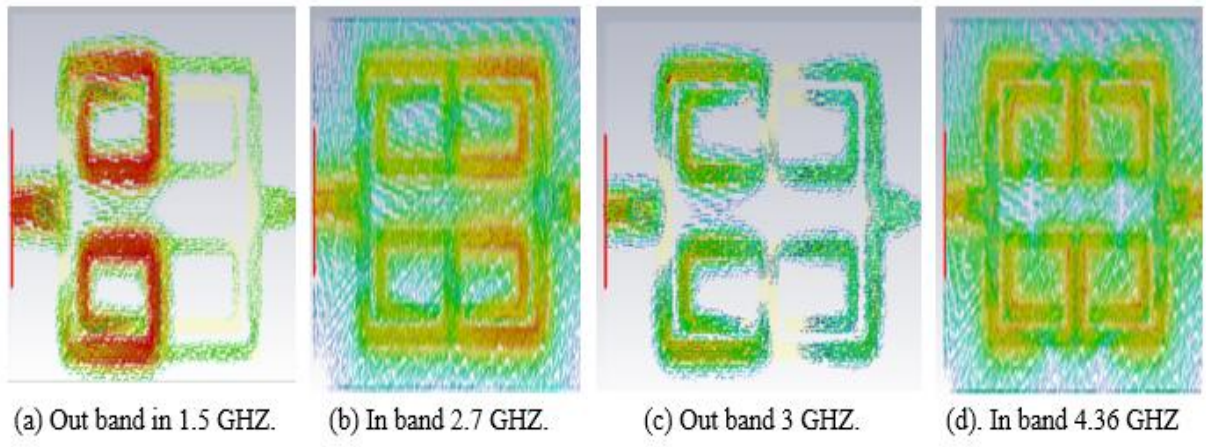

Figure 6. Presented the current distribution of four states when at multi frequencies for filter.

We can see ın Figure 8, it is shown frequency response that effect changed value of the width W1. For each of the four values of (w1), the poles. first. band are located at (2.5 , 2.8)GHz, with (S11) values of (-39.57 ,-35.23) dB,. respectively. The frequency range spans (2.5 - 2.9) GHz, with a central frequency. 2.6 GHz. The fractional bandwidth (Δf) is 18%. The second. band created (L5), hence the impact of altering (W) on this band is pretty evident. The BW ranges. (1.5 - 2.5) GHz, with a FBW (Δf) of 2.5%. There is a singular pole when (W1) measures 2 mm. According to the values of the poles.. in the . (S11) response, this pole is situated at 4.2 and 4.5. Considering the spectral positioning of the operational frequency bands and the transition slope characteristics derived from the forward transmission parameter (S21) analysis, reduced W1 dimensional values demonstrate suboptimal resonant band performance. Conversely, the resonant frequency response at w1=2.5 mm exhibits minimal reflection coefficient (S11) magnitude for both resonant poles, demonstrating effective electromagnetic coupling characteristics. Based on these analytical considerations, the loaded stub width parameter (W1) is optimally established at 2 mm.

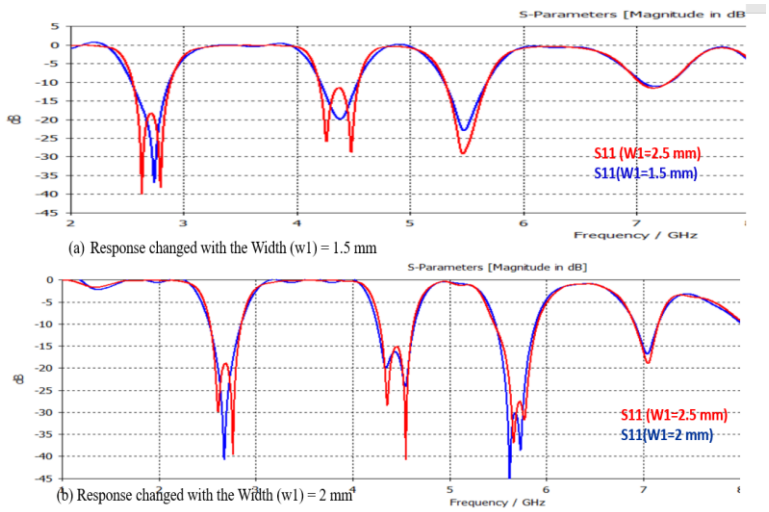

Figure 7. Simulated S-parameters of BPF changed with the width (w1).

The Figure 9 shown frequency response that effect changed value of the width W2. Across all four W2 dimensional configurations, the primary frequency band exhibits resonant poles positioned at 2.5 and 2.8 GHz, corresponding to reflection coefficient (S11) magnitudes of (-12.57 ,33.23) dB. respectively. The operational BW from 2.5 to 2.9 GHz with a central frequency 2.8 GHz, yielding a FBW (Δf). 22%. The tertiary frequency band emerges through L6 parameter influence, demonstrating significant sensitivity to W2 variations. This band spans from 1.5 to 2.5 GHz with a FBW(Δf) of 7%. A singular resonant pole manifests when W2 equals 2 mm, positioned at frequencies of 4.15 and 4.6 GHz. Evaluating the resonant pole characteristics within the input reflection parameter (S11) response, combined with spectral band positioning and transition slope characteristics from the forward transmission coefficient (S21) analysis, reduced W2 values exhibit degraded resonant band performance. The resonant configuration at w2=1 mm demonstrates optimal S11 suppression for both resonant poles with effective electromagnetic coupling. Based on these performance evaluations, the loaded stub width parameter (W2) is optimally configured at 1.4 mm, additionally enhancing return loss performance from 10 dB to 20 dB.

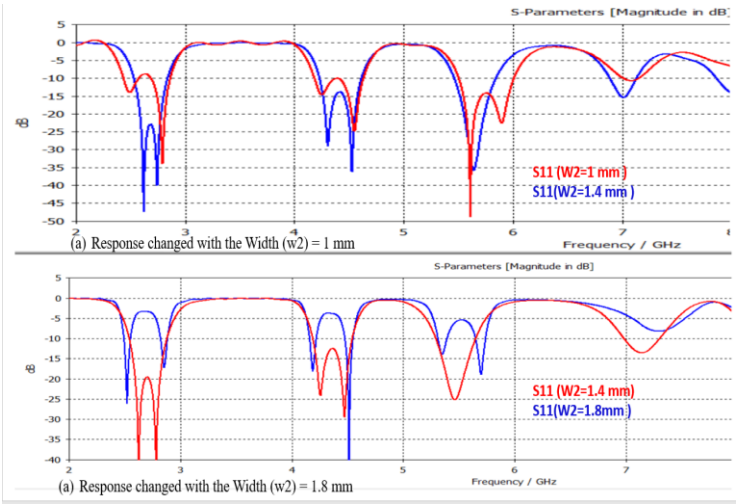

Figure 8. Simulated S-parameters of BPF changed with the width (w2).

In Figure 10, it is shown frequency response that effect changed value of the length L1. For any of the 4 values of (L1), the poles.in first band are located at (2.5, 2.6, 2.8) GHz, with corresponding S11 values of -39.57, -33.23, and -31.25 dB. The frequency range spans from 2.5 to 2.9 GHz, with a central frequency of 2.8 GHz. The FBW (Δf) is 18%. The Third pole generated. (L7), so the effect of varying. (L1) on this band is quite noticeable. A singular resonant pole emerges when the L1 parameter equals 17.5 mm, positioned at frequencies of 4.4 and 4.6 GHz. Evaluating the resonant pole characteristics within the input reflection parameter (S11) response, combined with spectral band positioning and transition slope characteristics from the forward transmission coefficient (S21) analysis, reduced L1 dimensional values demonstrate suboptimal resonant band performance. The resonant configuration at L1=18.5 mm exhibits minimal S11 magnitude for both resonant poles with effective electromagnetic coupling characteristics. Based on these performance assessments, the loaded stub length

parameter (L1) is optimally established at 18 mm, simultaneously enhancing return loss performance from 10 dB to 20 dB. Figure (10) conclusively demonstrates the correlation between L1 length variations and their corresponding impact on return loss characteristics.

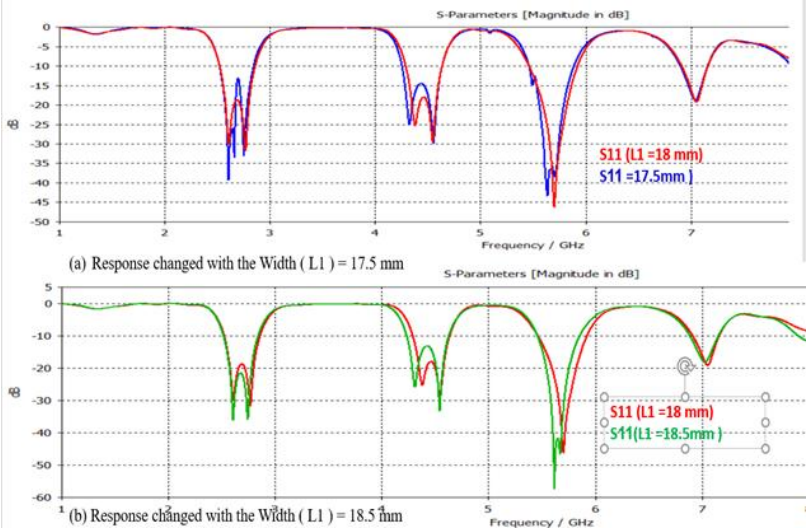

Figure 9. Simulated S-parameters of BPF changed with the width (L1).

Figure 11 illustrates the frequency response characteristics influenced by L2 length parameter variations. Across all four L2 dimensional configurations, the primary frequency band exhibits resonant poles positioned at 2.5 and 2.8 GHz, corresponding to reflection coefficient (S11) magnitudes of(-44.57 , -25.23) Db. serially . The operational BW (2.4 - 2.8) GHz with a central. frequency of 2.7 GHz, yielding a FBW (Δf) . 16%. A singular resonant pole manifests when L1 equals 2 mm, positioned at 2.6 GHz. Evaluating the resonant pole characteristics within the input reflection parameter (S11) response, combined with spectral band positioning and transition slope characteristics from the forward transmission coefficient (S21) analysis, reduced L1 dimensional values demonstrate suboptimal resonant band performance. The resonant configuration at L2=3.5 mm exhibits minimal S11 magnitude for both resonant poles with effective electromagnetic coupling characteristics. Based on these performance evaluations, the loaded stub length parameter (L2) is optimally established at 2.5 mm, simultaneously enhancing return loss performance from 30 dB to 45 dB. Figure 11 conclusively demonstrates the correlation between L2 length variations and their corresponding impact on return loss characteristics and fractional bandwidth at frequencies of (4.37 ,5.5)GHz.

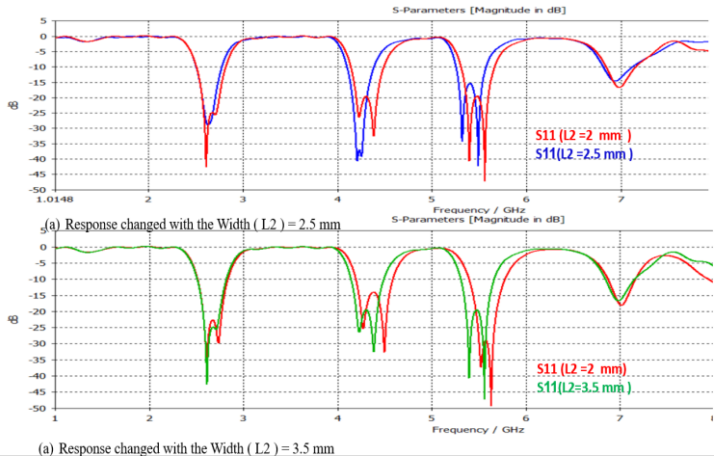

Figure 10. Simulation. S parameters BPF changed with the width (L2).

Frequency response shown in Figure 12, which expalain the effect changed size of the length L4. Throughout all four L4 dimensional configurations, the primary frequency band exhibits resonant poles positioned at 3.6 and 3.9 GHz, corresponding to reflection coefficient (S11) magnitudes of -26.57 and -29.23 dB respectively. The operational BW covers from 3.6 - 4.1 GHz in a central frequency of 3.9 GHz, yielding a FBW (Δf) of 20%. A singular resonant pole manifests when L4 equals 6 mm, positioned at frequencies of 3.50 and 3.8 GHz. Evaluating the resonant pole characteristics within the input reflection parameter (S11) response, combined with spectral

band positioning and transition slope characteristics from the forward transmission coefficient (S21) analysis, reduced L4 dimensional values demonstrate suboptimal resonant band performance. The resonant configuration at L4=6.5mm exhibits minimal S11 magnitude for both resonant poles with effective electromagnetic coupling characteristics. Based on these performance assessments, the loaded stub length parameter (L4) is optimally established at 7.2 mm., also improve retun loss from 10db to 22dB. In conclusion at Figure (12) when change length L2 That effect in the Return losses and fractal band width at 4.1GHz, 6.5GHz.In conclusion at Figure (12) when change length L4 That effect in the Return losses and position band 2.7 GHz become position at 3.5 GHz, 4.37 GHz become position at 5.8 GHz .

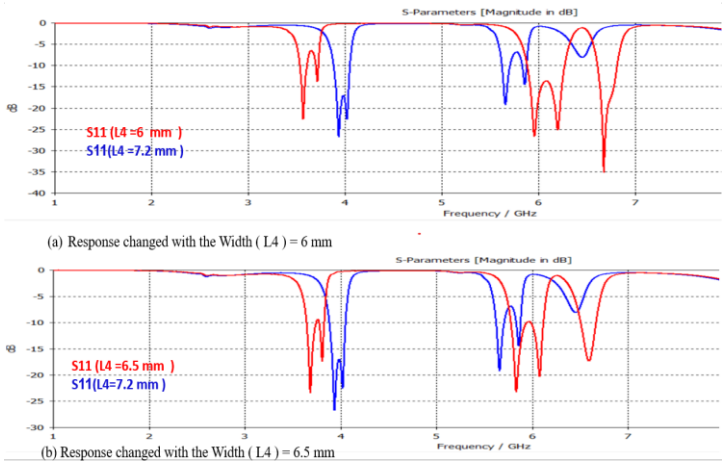

Figure 11. Simulated S-parameters of band pass filter changed with the width (L4).

Formore, Figure 13, it is shown frequency response that effect changed value of the length L5. Throughout the four investigated L5 length variations, dual resonant frequencies emerge at 3.75 and 3.9 GHz within the initial passband, demonstrating return loss magnitudes of -28.57 and -25.23 dB respectively. The transmission window spans 3.5 to 3.8 GHz, centered at 3.65 GHz, resulting in a relative bandwidth (Δf) of 19%. When L5 measures 11.5 mm, a single resonance occurs at 3.6 and 3.8 GHz frequencies. Analysis of resonant behavior through input return loss (S11) characteristics, alongside passband locations and selectivity slopes derived from insertion loss (S21) measurements, reveals that smaller L5 values produce inferior resonant performance. The L5=12.5mm configuration achieves superior S11 suppression for both resonances with strong inter-resonator coupling. Consequently, the optimal loaded stub length (L5) is determined to be 12 mm., also improve retun loss from 10db to 22dB. In conclusion at Figure (12) when change length L2 That effect in the Return losses and fractal band width at 4.1GHz, 6.5 GHz. In conclusion at Figure (13) when change length L5 That effect in the Return losses and position band 2.7 GHz become position at 3.5 GHz, 4.37 GHz become position at 5.95GHz.

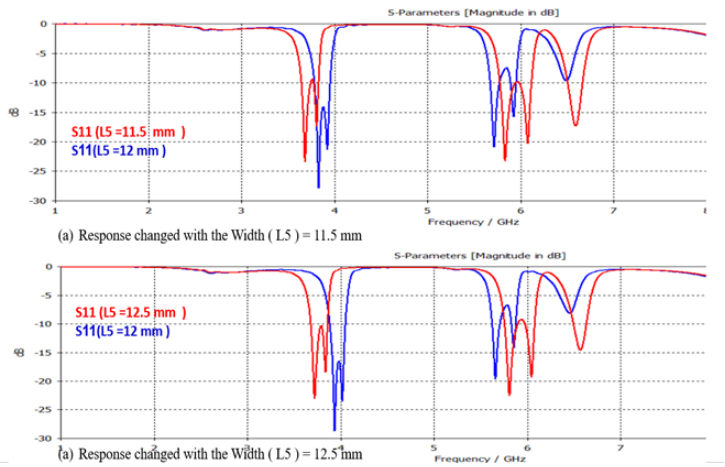

Figure 12.Simulated S-parameters of band pass filter changed with the length (L5).

Additionlly, Figure 14, it is shown frequency response that effect changed value of the length L6. Parametric analysis across four distinct L6 dimensional configurations reveals resonant mode excitation at 3.5 and 3.7 GHz frequencies within the fundamental transmission band, exhibiting input reflection coefficients of -24.57 and -20.23 dB respectively. The operational frequency spectrum encompasses 3.5 to 3.8 GHz. with a geometric mean

frequency of 3.65 GHz, yielding a normalized bandwidth coefficient (Δf) of 18.5%. Under L5=4.5mm geometric constraints, singular resonant mode manifestation occurs at 3.75 and 3.9 GHz spectral positions. Comprehensive evaluation of resonant pole characteristics through scattering parameter analysis (S11), integrated with spectral positioning assessment and transition gradient evaluation from forward transmission characteristics (S21), demonstrates that reduced L6 dimensional parameters result in degraded resonant band quality factors. The L6=5.5mm configuration demonstrates optimal input matching performance with enhanced electromagnetic coupling between resonant elements. Based on these comprehensive performance metrics, the loaded stub dimensional parameter (L6) is established at 5 mm for optimal circuit performance., also improve retun loss from 10db to 22dB. In conclusion at Figure (12) when change length L2 That effect in the Return losses and fractal band width at 5.5 GHz, 6.5 GHz. In conclusion at Figure (14) when change length L6 That effect in the Return losses and position band 2.7 GHz become position at 3.7 GHz only without change second band.

In Figure 15, it is shown frequency response that effect changed value of the length L7. The poles of the initial band for all four values of (L7) located. 4.3 and 4.6 GHz, with corresponding S11 values (-25 , -30) dB, respectively. The frequency range is from 4.15 to 4.7 GHz, in a center frequency of 4.65 GHz. The FBW (Δf) is 11%. There is only one pole when (L6) measures 8.5 mm. This pole is situated at coordinates 4.1, 4.3. Analysis of the pole values in the (S11) .response, in conjunction with the positioning of the relevant bands. , the roll-off. rate from the (S21). response, indicates that the low values of (L7) exhibit suboptimal resonant bands. The resonant band at (L7=9mm) exhibited the lowest S11 level for the two well-coupled poles. The value (L7) should 9.6 mm., also improve retun loss from 22db to 24dB. In conclusion at Figure (15) when change length L7 That effect in the Return losses and fractal band width at 4.45 GHz, 4. 6GHz and position band 4.1 GHz become position at 4.5 GHz only without change first band .

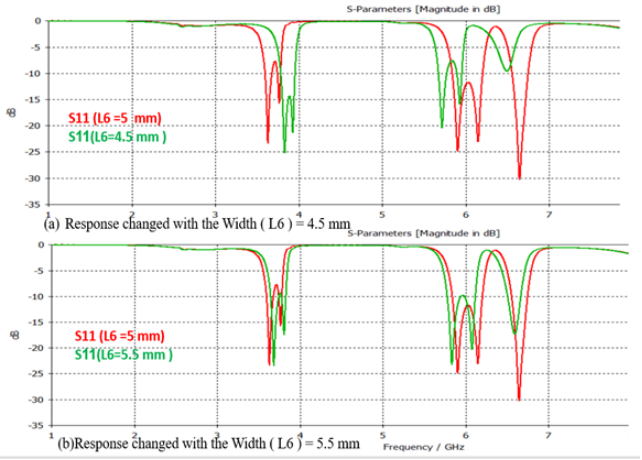

Figure 13. Simulated S-parameters of band pass filter changed with the width (L6).

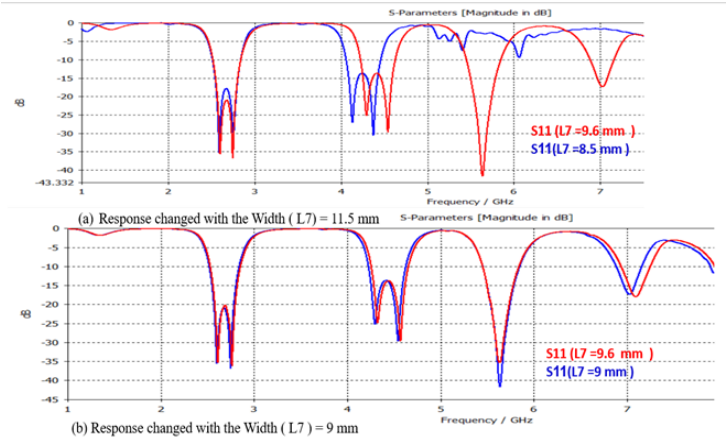

Figure 14. Simulated S-parameters of band pass filter changed with the width (L7).

Finally, Figure 17 displays the frequency responses that correspond to S11 and S21, the findings indicate that the bandpass filters derived from the initial meander -shape geometry iterations exhibit second-band characteristics, with transmission zeros situated at the first two bands, specifically at 2.6 GHz and 4.37 GHz, respectively. Simultaneously, there exists effective isolation among the two passbands. Simulation performed using CST

Roggerv43035c substrate with Er= 3.66, h = .762mm and tanδ = 0.0037 has been utilize to project the filter. The virtual frequency response for the prototype filter is shown at Figure 17 , where the simulated 3-dB FBW for the pass band, centered at 2.6GHz, is start to be 18% dB/GHz, 4.36 GHZ is found to be 11% , The LI is less than 0.2 dB. at 2.6 GHz and The IL is less than 0.6 dB at 4.37 GHz where as RL is greater than 16.6dB at 2.6 GHz and RL is big more than 11.3dB

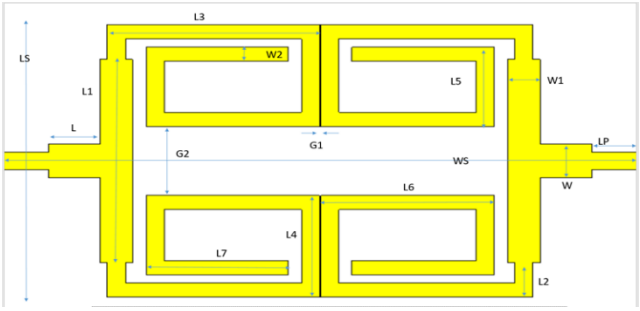

Figure 15. Final layout of second-order BPF

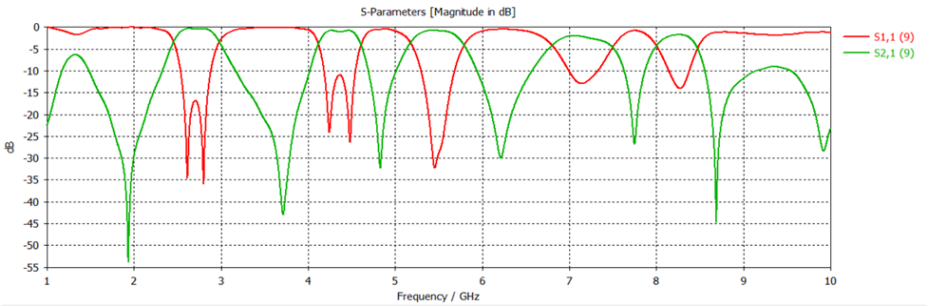

Figure 16. Final simulated results of S11 and S21 at the required bands

A trade. off exists between the filter project parameter. Since the future project had the lowest. IL, higher RL, highest. FBW, good. band. to range rejection. characteristics, its size is larger than the other topology cited in Table 2.

Table 2. Comparison with other works.

Ref	Pass bands	FBW %	IL (dB)	RL (dB)	dimensions ($\lambda g \times \lambda g$)	Technique
(Basit et al., 2023)	2.9−11.5	119.4	≤1.1	>10	0.32 × 0.08	SIR
(Sun et al., 2021)	2.65 4.84	6.04 8.70	≤0.99 ≤1.39	>15 >17	0.44 × 0.30	SLR
(Khani et al., 2019)	3.6 Tunable 5.7	-	≤0.53 ≤0.67	>25 >24.7	0.19 × 0.11	SIR
(Khani et al., 2017)	2.4 Tunable 5.7	-	≤0.64 ≤0.76	>20 >20	0.126 × 0.132	SIR
(Khani et al., 2020)	3.65 Tunable 5.67	11 26	≤0.62 ≤0.62	>20 >20	0.21 × 0.26	SIR
This work	Tunable 2.7 Tunable 4.37	18 11	0.2 0.6	>10 >20	0.72× 0.47	SIR

Table 3. Optimal dimensions of proposed DB BPF.

Parameter	Size (mm)	Parameter	Size (mm)
Wp=3.36	W2=1.4	L4=10	G1=0.1
LP= 4	L1=18	L5=12	G2=4.8
L=3.5	L2=2	L6=5	ε_r= 3.66
W1= 2.5	L3=15	L7=7=9.6	H= .762
WS=49	LS=30		

Conclusion

This paper has introduced compacted DBBPF which is collected of BPF1 and BPF2, built on the stepped impedance resonator (SIR) with The fundamental idea was to generate two operational passbands. the proposed filter demonstrates superior and distinguished performance, achieving ultra-low insertion losses of 0.2 dB and 0.6 dB for the first and second bands respectively-values significantly lower than most existing designs. Additionally, it offers high return losses of 16.7 dB and 11.3 dB, along with enhanced fractional bandwidths of 18% and 11% for both bands, highlighting its advanced capability. Moreover, the filter showcases advanced miniaturization while preserving high performance, with a compact footprint of 49 × 30 mm² (0.7λg × 0.47λg at 2.6 GHz). This is achieved by utilizing a carefully optimized meandering technique that balances size reduction and electrical performance—an ongoing challenge in modern filter design. A key innovation in this work is the quasi-independent control of each band, made possible through precise adjustment of stepped-impedance resonator (SIR) section lengths. This provides a high level of design flexibility, allowing each band to be tuned individually with minimal impact on the other, making the filter adaptable to diverse application requirements. Additionally, the strategic placement of transmission zeros at 1.93, 3.71, and 4.83 GHz enhances selectivity and inter-band isolation, resulting in excellent suppression of undesired frequencies. Finally, the design emphasizes practical application and manufacturability by employing the commercially available Rogers RO4350C substrate and relying on standard PCB fabrication processes. These choices not only ensure feasibility for mass production but also align the design with emerging technologies such as 5G and WLAN.

Recommendations

This study recommends the use of meandered-shaped stepped impedance resonators (MSIRs) for compact and high-performance dual-band bandpass filter designs in modern wireless communication systems. Future designs should incorporate quasi-independent tuning by adjusting the lengths of individual SIR sections to enable precise control of each passband with minimal interaction. Additionally, strategically placing transmission zeros near the desired bands—such as those demonstrated at 1.93, 3.71, and 4.83 GHz—can significantly enhance selectivity and inter-band isolation. Employing low-loss, commercially available substrates like Rogers RO4350C is also advised to ensure manufacturability and scalability for practical applications, including 5G and WLAN systems. Moreover, balancing size reduction with performance metrics such as insertion loss and return loss remains essential. Continued exploration of parametric variations in physical dimensions may yield further improvements in filter characteristics and broaden applicability across advanced RF systems.

Scientific Ethics Declaration

* The authors declare that the scientific ethical and legal principles have been strictly followed throughout the preparation and submission of this research. All data presented are original, and proper citation has been provided for previously published works. No part of this manuscript has been plagiarized or submitted elsewhere. The study does not involve any form of human or animal experimentation. The authors affirm that the work complies with the ethical standards of academic integrity and research conduct.

Conflict of Interest

* The authors declare that there is no conflict of interest regarding the publication of this paper. All authors have contributed to the work impartially, and no financial, personal, or professional relationships influenced the results or interpretation of the research.

Funding

* This research received no specific grant from any funding agency in the public, commercial, or not-for-profit sectors.

Acknowledgements or Notes

* This article was presented as an oral presentation at the International Conference on Engineering and Advanced Technology (ICEAT) held in Selangor, Malaysia on July 23-24, 2025.

* The authors would like to express their sincere appreciation to the College of Electrical and Electronic Engineering at the University of Technology for its continuous support and contribution to the success of this research. The authors would also like to extend their heartfelt thanks to Dr. Jabbar for his valuable supervision and technical insights, to Dr. Mohammed for his constructive feedback and academic support, and to Dr. Hussam for his helpful guidance and encouragement throughout the development of this work.

References

Alizadeh Pahlavani, M., Moradkhani, M., & Sayadi, R. (2020). New design of an adjustable compact microstrip lowpass filter using Z-shaped resonators with low VSWR. *Microwave and Optical Technology Letters*, *62*(11), 3527–3535.

Basheer, A., Abdulhussein, H., Al-Saedi, H., & Ali, J. K. (2022). Design of bandpass filter for 5G applications with high-selectivity and wide band rejection. *2022 Muthanna International Conference on Engineering Science and Technology (MICEST)* (pp. 179–183).

Basit, A., Daraz, A., Khan, M. I., Saqib, N., & Zhang, G. (2023). Design, modeling, and implementation of dual notched UWB bandpass filter employing rectangular stubs and embedded L-shaped structure. *Fractal and Fractional*, *7*(2), 112.

Bi, X., Ma, Q., Cao, Z., & Xu, Q. (2022). *Design and analysis of multi-band filtering circuits*. Springer Singapore.

Crnojević-Bengin, V. (Ed.). (2015). *Advances in multi-band microstrip filters*. Cambridge University Press.

Khani, H. I., Ezzulddin, A. S., Al-Saedi, H. H. A., Ezzulddin, A. S., & Al-Saedi, H. (2022). Design of a compact and highly independent triple-band BPF for 5G applications. *International Journal of Microwave and Optical Technology*, *17*(5), 524-532.

Khani, S., Danaie, M., & Rezaei, P. (2019). Miniaturized microstrip dual-band bandpass filter with wide upper stop-band bandwidth. *Analog Integrated Circuits and Signal Processing*, *98*(2), 367–376.

Khani, S., Danaie, M., Rezaei, P., & Shahzadi, A. (2020). Compact ultra-wide upper stopband microstrip dual-band BPF using tapered and octagonal loop resonators. *Frequenz*, *74*(1–2), 61–71.

Khani, S., Makki, S. V. A., Mousavi, S. M. H., Danaie, M., & Rezaei, P. (2017). Adjustable compact dual-band microstrip bandpass filter using T-shaped resonators. *Microwave and Optical Technology Letters*, *59*(12), 2970–2975.

Radhi, N., & Fadhil, M. (2023). Design of fractal-based tri-band microstrip bandpass filter for ISM, WLAN and Wimax applications. *International Journal of Wireless & Mobile Networks*, *15*(2/3), 09–14.

Riaz, L., Naeem, U., & Shafique, M. F. (2016). Miniaturization of SIW cavity filters through stub loading. *IEEE Microwave and Wireless Components Letters*, *26*(12), 981–983.

Seddiki, M. L., Nedil, M., & Ghanem, F. (2023). New design of reconfigurable stop-band in UWB band-pass filter based on resonator-loaded slot-line. *IETE Journal of Research*, *69*(3), 1356–1362.

Sun, M., Chen, Z., Zuo, T., Zuo, Z., & Zhang, A. (2021). A high selectivity dual-band bandpass filter using quadruple-mode multi-stub loaded ring resonator (SLRR). *International Journal of RF and Microwave Computer-Aided Engineering*, *31*(7), e22667.

Author(s) Information

Enas S. Mohammed
University of Technology - Iraq, Department of Electrical and Electronic Engineering, Iraq
Contact e-mail: *eee.20.23@grad.uotechnology.edu.iq*

Mohammed F. Hasan
University of Technology - Iraq, Department of Electrical and Electronic Engineering, Iraq

Jabber K. Mohammed
University of Technology - Iraq, Department of Electrical and Electronic Engineering, Iraq

To cite this article:

Mohammed, E. S., Hasan, M. F., & Mohamed, J. K. (2025). Band pass filter utilizing a stepped impedance resonator for modern wireless communication system *The Eurasia Proceedings of Science, Technology, Engineering and Mathematics (EPSTEM), 37*, 444-456.